



HAL
open science

Calcium phosphate mineralization through homogenous enzymatic catalysis: Investigation of the early stages

E. Colaço, D. Brouri, C. Méthivier, L. Valentin, F. Oudet, K. El Kirat, C. Guibert, J. Landoulsi

► To cite this version:

E. Colaço, D. Brouri, C. Méthivier, L. Valentin, F. Oudet, et al.. Calcium phosphate mineralization through homogenous enzymatic catalysis: Investigation of the early stages. *Journal of Colloid and Interface Science*, 2020, 565, pp.43 - 54. 10.1016/j.jcis.2019.12.097 . hal-03489538

HAL Id: hal-03489538

<https://hal.science/hal-03489538>

Submitted on 7 Mar 2022

HAL is a multi-disciplinary open access archive for the deposit and dissemination of scientific research documents, whether they are published or not. The documents may come from teaching and research institutions in France or abroad, or from public or private research centers.

L'archive ouverte pluridisciplinaire **HAL**, est destinée au dépôt et à la diffusion de documents scientifiques de niveau recherche, publiés ou non, émanant des établissements d'enseignement et de recherche français ou étrangers, des laboratoires publics ou privés.



Distributed under a Creative Commons Attribution - NonCommercial 4.0 International License

Calcium phosphate mineralization through homogenous enzymatic catalysis: investigation of the early stages

E. Colaço ^a, D. Brouri ^b, C. Méthivier ^b, L. Valentin ^b, F. Oudet ^c, K. El Kirat ^a, C. Guibert ^b, J. Landoulsi ^{a, b*}

^a *Laboratoire de Biomécanique & Bioingénierie, CNRS, Université de Technologie de Compiègne, BP 20529, F-60205 Compiègne Cedex, France*

CNRS 7154, 75205 Paris Cedex 05, France

^b *Sorbonne Université, CNRS, Laboratoire de Réactivité de Surface, F-75005 Paris, France*

^c *Service d'analyse physico-chimique, Université de Technologie de Compiègne, BP 20529, F-60205 Compiègne Cedex, France*

* corresponding author: jessem.landoulsi@sorbonne-universite.fr

Abstract

Hypothesis: The crystallization of calcium phosphate (CaP) is a ubiquitous process that occurs in several mineralized tissues and involves a variety of biochemical and chemical reactions. This issue has been hitherto continuously studied from supersaturated solutions (*chemical* procedure), i.e. by adding calcium and orthophosphate ions in a homogenous phase. Yet, both *in vivo* and *in vitro* investigations have clearly shown the implication of enzymes, namely alkaline phosphatase (ALP), to initiate the mineralization process by generating orthophosphate ions.

Experiments: We report a thorough investigation on the mechanism of enzyme-induced mineralization in homogenous phase (*enzymatic* procedure). For this purpose, ALP is introduced in Ca²⁺/Mg²⁺-containing solution (pH = 7.4; 37 °C), and its activity modulated by the concentration of its substrate.

Findings: Results show that after 24 h of mineralization both *chemical* and *enzymatic* procedures lead to the formation of well-crystalline hydroxyapatite nano-objects, however with noticeable impact on their shape and dimensions. Remarkably enough, by combining *in situ* monitoring and *ex situ* characterizations, we identify several intermediate phases, including amorphous phase, dicalcium phosphate dehydrate phase (DCPD or brushite) and Whitlockite (WH). Besides, mineralized nano-objects with a core-shell structure is observed, and hydroxyapatite platelets are shown to grow on the surface of their shell.

Keywords: biomineralization; enzyme; hydroxyapatite; Whitlockite; XPS; DLS

1. Introduction

Calcium orthophosphates (CaP) are the main mineral constituents of vertebrate bones and teeth.[1] They may also form during pathological calcification, such as in kidney stones and in articular cartilage.[2,3] CaP compounds have been the subject of a vast literature owing to the diversity of mechanisms determining their growth, dissolution and phase transformations.[4] *In vitro*, CaP compounds are often obtained from supersaturated solutions, i.e. through the precipitation of calcium and orthophosphate ions in a homogenous phase under different physicochemical conditions (pH, temperature, ionic strength), also in the presence of (bio)organic molecules.[5–8] Hydroxyapatite (HAP) is the least soluble phase at physiological pH. [9] The crystallization process of HAP involves several transition phases the occurrence of which is governed by both thermodynamic and kinetic factors. [4] Particularly, the formation of metastable amorphous calcium phosphate (ACP) from supersaturated solutions has been well-documented. [10–12] Octacalcium phosphate (OCP) has been also proposed as a precursor during the crystallization of HAP under neutral or basic conditions. [9] At slightly acidic pH (below pH ~6.5), dicalcium phosphate dehydrate phase (DCPD or brushite) has been reported as an intermediate to the formation of HAP. [4] The detection of all these intermediates and the precise identification of their nature remain tricky, owing to their instability and the need of tools to resolve, in real-time, morphological and/or phase transformations.

In vivo, the mechanism of HAP formation is more complex. CaP biomineralization involves several physicochemical and biochemical processes that lead to the formation of apatite mineral within collagen fibrils located in the extracellular matrix.[13] Although the precise mechanisms of nucleation and growth of HAP remain under debate, it is well-established that extracellular matrix vesicles (MV, typically ~20-200 nm), are the site where CaP compounds nucleate. [14] This is mainly achieved through two processes. (i) Lipids, present on the MV

surface, can bind Ca^{2+} ions and their internalization is then facilitated by protein transporters through membrane channels, and (ii) tissue non-specific alkaline phosphatase (ALP) catalyzes the production of orthophosphate ions as follows:



Although disparate views regarding the mechanism of the early stages of mineralization associated to MVs [14] or to intrafibrillar collagen mineralization [15] are still described in the literature, the implication of ALP in the formation of mineral is now well-established. [16] The ALP activity has indeed become a standard protocol to evaluate the ability of cells to mineralize their extracellular matrix during *in vitro* tests. [17] ALP initiates the first step of the mineralization process by the hydrolysis of inorganic pyrophosphate, originating from extracellular nucleoside triphosphate, occurring inside the MVs. [18] It has been suggested that minerals form within the vesicles that subsequently breakdown, probably through hydrolysis, leading to the release of CaP particles in the extracellular fluid.[14,19] The fate of these mineralized particles remains, however, unclear, but these findings have motivated the use of ALP in biomimetic systems to initiate the formation of mineral *in vitro*. [20–24] Nevertheless, the precise pathways of enzyme-induced mineralization and the role and nature of intermediate phases are still unknown. The stability of these intermediates is influenced by additional ions present in the surrounding medium, particularly Mg^{2+} [11]. This ion may stabilize ACP phase and can be present in the final apatite lattice as an ion substitute [9,11]. Moreover, Mg^{2+} ions act as activators and enhance the catalytic activity of ALP. [25]

In this paper, we investigate the mechanism of CaP mineralization using purified enzymes in homogenous phase. For this purpose, ALP is used to generate *in situ* orthophosphate ions in the aqueous solution (pH = 7.4, T = 37 °C) in the presence of Ca^{2+} and Mg^{2+} ions. A particular attention is dedicated to the effect of the catalytic activity on the mineralization process through the modulation of the concentration of the enzyme substrate. The evolution of

particle size during mineralization is monitored *in situ* by means of dynamic light scattering (DLS), their morphology characterized by transmission electronic microscopy (TEM) and their crystallinity evaluated by selected area electron diffraction (SAED) and X-ray diffraction (XRD). The chemical composition of the mineralized structures is determined by means of IR and X-ray photoelectron spectroscopy (XPS).

2. Materials and methods

2.1. Materials

Alkaline phosphatase from bovine intestinal mucosa (ALP, ≥ 10 U/mg), sodium phosphate dibasic (Na_2HPO_4 , $\geq 99\%$) calcium chloride (CaCl_2 , $\geq 99\%$), α -glycerol phosphate magnesium salt hydrate ($\sim 85\%$), 4-nitrophenyl phosphate disodium salt hexahydrate (pnpp, $\geq 99\%$) and 4-nitrophenol (pnp) were purchased from Sigma-Aldrich (France). Hydrochloric acid (HCl, 37%) was purchased from VWR (France) and sodium hydroxide (NaOH, 9.31 M) from Volusol (US/Canada). All solutions were prepared in ultrapure water (MilliQ, Millipore, France).

2.2. Mineralization procedures

The chemical procedure (*Chem*) was carried out as follows: a solution of CaCl_2 (11.4 mM) was prepared in ultrapure water. Na_2HPO_4 was then added to give rise to a final concentration of 7.0 mM. The solution was vigorously stirred and the pH adjusted to 7.4 with addition of NaOH (0.1 M). The mixture was stirred for 24 h at 37°C. The white precipitate was centrifuged, washed three times with ultrapure water and dried at 60°C.

The enzyme-induced mineralization (*Ez*) was performed as follows. A solution of CaCl_2 (11.4 mM) was prepared in ultrapure water. The substrate of the enzyme, α -glycerophosphate (see Eq. 1, where R is a glycerol moiety), was then added to give rise to a final concentration of $[\text{S}] = 0.7, 7.0$ or 70 mM. This substrate was used because the glycerol moiety is not expected to interfere with the CaP crystallization process. ALP was subsequently introduced at a final

concentration of 0.1 mg/mL. The solution pH was finally adjusted to 7.4 and the mixture was gently stirred at 37 °C during 24 h. The solution was then centrifuged (6000 rpm for 10 min at room temperature), washed three times with ultrapure water and dried at 60 °C. For the characterization of the intermediate phases, after a given time (10; 60; 130 and 235 min), the mineralization solution was placed in an ice bath to stop the ALP activity. The solution was then centrifuged, washed and dried following the same procedure described above.

2.3. Enzyme assay

ALP activity was evaluated by monitoring the production of pnp. Measurements were performed in aqueous solution (pH = 7.4) at 37 °C in the presence of pnp substrate (Eq. 1, where R is a nitrophenol moiety) at different concentrations ($[S] = 0.7, 7.0$ and 70 mM), while keeping Ca^{2+} concentration unchanged ($CaCl_2$ 11.4 mM). The pnp concentration was determined by measuring the absorbance at 410 nm using a UV-Vis spectrophotometer (Biochrom). A calibration curve was preliminarily established to relate the absorbance at 410 nm to pnp concentration.

2.4. DLS

The DLS correlograms were recorded using the Zetasizer Nano ZS instrument (Malvern, France). The measurements were carried out while the crystallization was taking place in the DLS cuvette. The time $t = 0$ corresponds to the first measurement that was performed right after the addition of the enzyme to the rest of the system, already in solution.

The CONTIN algorithm of the Zetasizer software was used to fit the measured correlograms. DLS is a technique that allows measuring the intensity-weighted size distribution of particle dispersions. It is then extremely sensitive to very small quantities of aggregates, as the size distributions are proportional to the sixth power of the particle size. In order to give a more representative result, the hydrodynamic diameters d_H reported here correspond to the values of the intensity-weighted distribution peaks, taking into account their relative amount in

extrapolated number-weighted distributions. Above ca. 1 μm the hydrodynamic diameters determined for this kind of system correspond to big aggregates the size of which cannot be very well determined through this technique.

2.5. TEM

TEM micrographs were recorded using a JEOL JEM-2100F instrument (Japan) operating at an acceleration voltage of 200 kV equipped with a CCD camera for micrograph acquisition. The crystallinity of CaP particles was analyzed using selected area electron diffraction (SAED) mode and high-resolution transmission electron microscopy (HRTEM). All the samples were prepared as described above (section 2.2.), and the obtained solid was dispersed in ultrapure water, deposited (a drop of 10 μL) onto a copper-mesh grid coated with an amorphous carbon film, then allowed to air-dry (~45 min) before visualization.

2.6. XRD

The crystalline structures of the compounds in a powdery form were identified by XRD using a Bruker D8 Advance Instrument with a Cu-K α radiation source ($\lambda = 0.15418 \text{ nm}$) and Ni filter under ambient conditions. The samples were finely ground before measurement and deposited on a silicon single crystal support. The analysis was operated at a 2θ range from 10 to 80°. The crystalline phases of the products were determined by comparison with the diffraction database from the reference JCPDS files.

2.7. XPS

XPS analyses were performed using an ESCA+ spectrometer (Omicron Nano-Technology) equipped with a monochromatized aluminum X-ray source (powered at 20 mA and 14 kV) and an MCD 128 channeltron detector. Charge stabilization was ensured using a CN10 device with an emission current of 5.0 μA and a beam energy of 0.30 eV. Analyses were performed in sweep mode; the resulting analyzed area was 1 mm in diameter. A pass energy of 20 eV was used for narrow scans. Under these conditions, the full width at half-maximum (FWHM)

of the Ag 3d_{5/2} peak of a clean silver reference sample was about 0.6 eV. The pressure in the analysis chamber was approximately 10⁻¹⁰ Torr. Samples (powder) were fixed on an indium foil. Unless stated elsewhere, the photoelectron collection angle, θ , between the normal to the sample surface and the analyzer axis was 45°. The following sequence of spectra was recorded: survey, C 1s, O 1s, N 1s, P 2p, Ca 2p, Mg 2s and C 1s again to check for charge stability as a function of time and the absence of sample degradation. The binding energy scale was set by fixing the C 1s component due to carbon bound to only carbon and hydrogen at 284.8 eV. The data treatment was performed with CasaXPS software (Casa Software Ltd., Teignmouth, U.K.). The peaks were decomposed using a linear baseline and a component shape defined by the product of a Gaussian function and a Lorentzian function in a 70:30 ratio. Molar fractions were calculated using peak areas normalized according to Scofield factors.

2.8. IR analyses

Diffuse reflectance infrared (DRIFT) analyses were performed on powdered samples corresponding to a mixture of CaP and KBr (20/80, wt./wt). The sample was placed in a crucible equipped with two ZnSe windows. Spectra were obtained by the sum of 64 scans at 4 cm⁻¹ resolution using KBr as reference. All analyses were recorded in ambient conditions using a Brüker Vector 22 V spectrometer equipped with a DTGS detector.

3. Results and discussion

3.1. Catalytic activity

The catalytic properties of ALP were investigated in the aqueous solution (CaCl₂ 11.4 mM, pH = 7.4) by means of the pnp method, as described above. The activity was measured at 37 °C at a fixed ALP concentration (0.1 mg/mL) while varying the concentration of the substrate over a range of 0.7 to 70 mM. A typical evolution of the absorbance ($\lambda = 410$ nm) vs time is given in Fig. 1A. A calibration curve was preliminarily drawn to relate the absorbance to pnp

concentration (Fig. 1A, inset). The evolution of the pnp production vs time is given in Fig. 1B at substrate concentrations $[S] = 0.7, 7.0$ and 70 mM. It is shown that the concentration of pnp increased progressively as a result of the ALP-catalyzed reaction (Eq. 1). A fast increase was first observed: it corresponds to the initial activity of enzymes (linear portion of the curve). The slope of pnp production decreased then as a function of time, indicating a decrease of the enzymatic reaction kinetic, to reach a plateau after about 10 to 50 min, depending on the initial concentration of the substrate (Fig. 1B). This evolution is due to the enzyme inhibition due to orthophosphate ions, [26], which may be influenced, in this case, by the presence of Ca^{2+} ions in the medium, and thus the CaP precipitation reaction. The initial activity, v , was thus determined by applying a linear fit and expressed in pnp concentration (μM) produced per minute. The activity-substrate concentration relationship of ALP used in the present study was satisfactorily consistent with the classical Michaelis-Menten model ($K_m = 8.1$ mM, Fig. 1C, inset), in agreement with previous findings [27]. When considering a possible allosteric effect, due to the presence of two active sites ($n = 2$) in the homodimer, [27,28], fitting parameters yield a constant value, analogous to K_m , of about 7.5 mM (Fig. 1C).

These findings clearly show that the ALP activity is highly influenced by the substrate concentration in the studied conditions, namely at $[S] = 0.7, 7.0$ and 70 mM. Accordingly, this way of modulating the enzymatic activity will be explored in the mineralization tests, i.e. in the presence of Mg^{2+} ions and using α -glycerol phosphate as a substrate, to evaluate its impact on the crystallization process.

3.2. Chemical vs enzymatic mineralization

The morphologies of CaP particles obtained using the *Chem* and *Ez* procedures after 24 h of mineralization are presented in Fig. 2 and summarized in Table 1. TEM micrograph showed that the nano-objects obtained by the *Chem* procedure mostly exhibit flat rod-like structure with a length of 75 ± 7.5 nm and width of 16.4 ± 2.4 nm (Fig. 2A). The enzyme-induced

mineralization, E_z , was performed using the three substrate concentrations studied above, i.e. $[S] = 0.7, 7.0$ and 70 mM, as suggested above. When using $[S] = 0.7$ mM, the mineralized particles showed well-defined platelets of $61.3 (\pm 9.6)$ nm in length and $43.9 (\pm 5.4)$ nm in width (Fig. 2B). At $[S] = 7.0$ mM, TEM image also showed larger platelet-shaped particles, with $144.8 (\pm 23.4)$ nm in length and $73.8 (\pm 10.5)$ nm in width (Fig. 2C). The aspect ratio, which reflects the anisotropic feature of the nano-object, calculated on the particles obtained using the *Chem* procedure was significantly higher compared to those obtained when using the E_z procedure at $[S] = 0.7$ and 7.0 mM (Table 1). By contrast, the situation was radically different at $[S] = 70$ mM. The mineralized particles did not exhibit well-defined shape and appeared highly aggregated (Fig. 2D).

Regarding the crystal phase of the mineralized particles, SAED patterns obtained for the *Chem* procedure showed several distinct diffraction rings (002), (210), (202), (302), (213), (004) and (313) which are typical of well-crystalline HAP (Fig. 2E). Similar SAED patterns of HAP were also observed with $[S] = 0.7$ mM and $[S] = 7.0$ mM, even if some planes were not observed in both patterns, most likely because of different orientations of the nano-objects (Figs 2F and G). By contrast, with $[S] = 70$ mM, no noticeable spots were observed in SAED pattern suggesting the presence of an amorphous phase (Fig. 2H).

XRD analysis supports the observations made with SAED. Results showed well-defined peaks typical of the hexagonal lattice of HAP when using the *Chem* procedure (Fig. 3). Similar patterns were also obtained using the E_z procedure at $[S] = 0.7$ and 7.0 mM and no additional phases were detected. By contrast, a typical signature of ACP was observed at $[S] = 70$ mM with a broad pic around $2\theta = 30^\circ$. To compare the degree of crystallinity of HAP particles, obtained in the former cases, an empirical index of crystallinity was calculated from surface area of (002) peak (I_{002}) and the contribution of the background in the same area (I_{bgr}), as follow: Index of crystallinity = $(I_{002} - I_{bgr})/I_{002}$. Results showed that *Chem* procedure leads

to better crystallinity with an index of 0.62 (Table 1). We can also notice that the crystallinity increased for increasing [S] from 0.7 mM to 7.0 mM (crystallinity index of 0.41 and 0.53 respectively), and fell down for higher concentrations [S] where the sample is amorphous for [S] = 70 mM (Table 1). It must be kept in mind that the method adopted here does not provide absolute degree of crystallinity but allows samples to be compared with each other.

The main characteristics of the mineralized nano-objects obtained through the *Chem* or the *Ez* procedure are summarized in Table 1. Although they exhibited the same crystal phase, HAP, except the amorphous one, they noticeably differ by their shape and aspect ratio.

The composition of the different CaP nano-objects was investigated using DRIFT analyses. All the spectra showed characteristic bands of CaP compounds (Fig. 4). The bands at 1086 and 1025 cm^{-1} are due to the asymmetric stretching mode $\nu_3(\text{PO}_4^{3-})$. The symmetric stretching mode $\nu_1(\text{PO}_4^{3-})$ was also visible at 961 cm^{-1} . [29,30] The bending mode, $\nu_4(\text{PO}_4^3)$, appeared as split bands at ca. 600 and 560 cm^{-1} in all the samples, as observed for HAP in previous works. [29,30] By contrast, only a broad band was observed in this region for the sample obtained at [S] = 70 mM, which may be attributed to its amorphous state. [31] The presence of HPO_4^{2-} ions was also detected at 865 cm^{-1} , the stretching mode $\nu_1(\text{HPO}_4^{2-})$, in all the crystalline samples (Fig. 4).

On the samples obtained via the *Ez* procedure at [S] = 0.7 mM and [S] = 7.0 mM, additional bands at 1657 cm^{-1} and 1540 cm^{-1} were observed (Fig. 4). They may be due to amide I and amide II, respectively, and may be attributed to peptidic link. The amide bands were not observed in samples obtained with the *Chem* procedure, and the one obtained via the *Ez* procedure at [S] = 70 mM. Instead, a single band due to $\delta(\text{H}_2\text{O})$ was observed at 1650 cm^{-1} . These results suggest the presence of adsorbed enzymes on the solid for samples obtained via the *Ez* procedure at [S] = 0.7 and 7.0 mM.

XPS analysis was also performed on the different mineralized nano-objects. Representative O 1s, N 1s and C 1s peaks are presented in Fig. 5. On the sample obtained with the *Chem* procedure, the C 1s peak exhibited a shape which is typical of adventitious organic contamination present on the surfaces of inorganic solids, [32,33] with a main contribution at 284.8 eV, due to carbon only bound to carbon and hydrogen. This component was used for the calibration of binding energy scale. Noticeable changes in the O 1s, N 1s and C 1s peak shapes were observed as a result of the procedure used (*Chem vs Ez*) and the substrate concentration (Fig. 5). The shape of the peaks results, indeed, from the superposition of components associated to the chemical functions in which the atom of interest is involved. Therefore, peak decomposition provides information on the chemical nature of the compounds probed by XPS. [34] The C 1s peak was decomposed using guidelines detailed in our previous studies. [35] The C 1s peak was decomposed in four components the FWHM of which were imposed to be equal: (i) a component at 284.8 eV, attributed to carbon only bound to carbon and hydrogen [C-(C,H)]; (ii) a component at 286.3 eV, assigned to carbon making a single bond with oxygen or nitrogen [C-(O,N)]; (iii) a component at 288.0 eV, assigned to carbon making one double bond or two single bonds with oxygen (C=O, O-C-O); and (iv) a component near 289.0 eV, assigned to carboxyl or ester functions [C-(C=O)-O] or to carbonate [O-(C=O)-O]. The N 1s peak did not show a noticeable contribution on the *Chem* sample. By contrast, on *Ez* samples, a main component around 399.8 eV, attributed to non-protonated amine or amide, was observed with a possible minor contribution at higher binding energy, near 401.5 eV, attributed to protonated amine. The O 1s peak showed a major contribution at 531.0 ± 0.2 eV and a weak component around 532.8 ± 0.4 eV. The interpretation of O 1s is particularly complex owing to the overlapping of components from organic and inorganic nature. Indeed, on phosphate-containing compounds, such as CaHPO₄, the O 1s peak was reported to show two components at about 531.3 and 532.9 eV attributed to

P=O or P-O⁻ and to P-OH, respectively. The component at about 531.0 eV is also attributed to oxygen making a double bond with carbon (C=O), including amide and carboxyl and to oxygen of carboxylate. A contribution above 532.6 eV can be attributed to oxygen of organic nature, as detailed in our previous study. [35]

Typical Ca 2p, P 2p and Mg 2s peaks are presented in Fig. S1 (Supporting information). Ca 2p peak showed a characteristic doublet of Ca^{II} compounds at 347.1 and 350.6 eV due to the Ca 2p_{3/2} and Ca 2p_{1/2} contributions, respectively. P 2p peak showed a contribution at about 133.2 eV, due to phosphate species, including P 2p_{3/2} and P 2p_{1/2} contributions. The concentrations associated to elements and functions defined by peak components are given in Table 2.

The significant increase of the molar concentration of nitrogen observed on the samples obtained by the *Ez* procedure, particularly at [S] = 0.7 and 7.0 mM (Fig. 5), may be explained by the presence of adsorbed proteins onto the solid, as observed by IR analyses (Fig. 4). Fig. S2 presents the plot of the concentrations of C₂₈₈ vs the concentration of nitrogen (N_{tot}). The regression lines were computed by considering only CaP samples obtained via the *Ez* procedure (circle symbols). The slope of 0.9 is close to the value expected for ALP (0.8, Table S4). The excellent correlation between the variation of N 1s and C 1s peak components attributed to peptidic links confirms the presence of proteins onto the CaP solids. Moreover, it is shown that the amount of adsorbed proteins on the final solid, i.e. after 24 h, depends on the substrate concentration following this trend: [S] = 0.7 mM > 7.0 mM > 70 mM (Fig. S2, Supporting information). This trend may be explained by the fact that the amount of mineral, the solid on which protein adsorption may occur, increases appreciably when increasing the enzymatic activity, while the concentration of free enzymes in the solution was kept unchanged (0.1 mg/mL).

Regarding the composition of the inorganic phase, as detailed in Supplementary Information (Section S1), experimental molar concentrations corrected from an organic continuous adlayer (from adventitious contamination or adsorbed proteins) yield a Ca/P ratio lower than the theoretical one expected for bulk HAP, 1.67. This result could be expected, as it corresponds to an average value over the depth scale probed by XPS (i.e. a few nm). Hence, XPS does not measure the composition of the particle core and it is very sensitive to interface alterations. It has been reported that hydroxyapatite may undergo a selective calcium desorption, leading to a surface depleted in calcium. [36] It is noteworthy that presence of carbonate at the surface of the different CaP solids, even weak, could not be excluded. This is shown by the low intensity of the C 1s component at high binding energy (around 289.0 eV, Fig. 5), and the weak contributions in the 1400-1550 cm^{-1} region in the DRIFT analyses (Fig. 4).

3.3. Enzyme-induced crystallization pathway

The kinetics of the crystallization process at early stages was studied by DLS. The corresponding hydrodynamic diameter d_H of the objects analyzed in the suspensions are plotted as a function of time in Fig. 6 for $[S] = 0.7 \text{ mM}$ and $[S] = 7.0 \text{ mM}$. The evolution of d_H measured for $[S] = 70 \text{ mM}$ is not represented here as objects larger than $1 \text{ }\mu\text{m}$ were found right after the introduction of the enzyme. Similar experiments were also performed for the *Chem* procedure but, in this case also, the mineralization process happened very fast and, due to the very large size of the particles quickly formed and to their number, no relevant data could be drawn from this experiment.

For $[S] = 0.7 \text{ mM}$ and $[S] = 7.0 \text{ mM}$, a quick increase of the size (0.7 mM: a few minutes, 7.0 mM: less than 20 min) was first observed. The system reached then a quite stable regime (0.7 mM: size around 200 nm, 7.0 mM: size around $500 \text{ nm} \pm 100 \text{ nm}$). A drastic increase of the size, rapidly above $1 \text{ }\mu\text{m}$, was finally observed (0.7 mM: after 80 min, 7.0 mM: after 180 min).

When enzyme samples are studied in these conditions without the addition of the substrate, a size distribution peak for the enzyme monomer or oligomer can be observed around 20 nm, which may suggest that the enzyme is predominantly in the tetrameric form (see the characteristic size of the protein in Fig. S3, Supporting Information). Interestingly enough, as soon as the enzyme is added, except for the very first measurement ($t = 0$) at $[S] = 0.7$ mM, no secondary size distribution peak was observed. Two explanations can be given for the disappearance of this peak: (i) it could be masked by the much more intense scattering of the bigger objects that are quickly formed during the crystallization, or (ii) its disappearance could be due to the aggregation of the enzymes into or onto bigger objects.

It must be noted that an appreciable multiple scattering phenomenon is taking place in the samples (y-intercept between 0.4 and 0.6 for $[S] = 0.7$ mM and between 0.6 and 0.7 for $[S] = 7.0$ mM, see Fig. S4, Supporting information): the sizes displayed in Fig. 6 are then most probably underestimated. Moreover, for $[S] = 7.0$ mM, the slight increase of d_H as a function of time between 20 min and 160 min could be an artifact due to the decrease of the multiple scattering (increase of the y-intercept) correlated with the possible sedimentation of the biggest scatterers. However, in the other sample ($[S] = 0.7$ mM), the evolution between 10 and 80 min cannot be explained in the same way, as the multiple scattering seems to increase with time.

In order to get a better understanding of the mechanisms at stake during the first stages of the mineralization, intermediate samples were withdrawn during the mineralization at characteristic times that correspond to the different mineralization regimes observed by DLS: 10 min, 60 min, 130 min and 235 min (Fig. 6). These aliquots were then immediately placed in an ice bath to stop the ALP activity, as described above (section 2.2). The evolution of the morphology of calcium phosphate particles that form via the *Ez* procedure at $[S] = 0.7$ mM and $[S] = 7.0$ mM over the mineralization time was assessed by means of TEM (Fig. 7A-H).

When introducing $[S] = 0.7 \text{ mM}$, clusters of around 10 nm were observed after 10 min of mineralization (Fig. 7A) and start agglomerating after 60 min (Fig. 7B). Subsequently, the particles evolved into amorphous globular nano-objects with an average diameter of about 77 nm, after 130 min (Fig. 7C). Subsequently these amorphous particles turned into needle-like particles after 235 min (Fig. 7D) which evolved, after 24 h, into platelets of lower aspect ratio (Fig. 2B). SAED pattern showed that the needle-like particles correspond to crystalline HAP phase (Fig. 7D, inset). The evolution of particle morphology was similar at $[S] = 7.0 \text{ mM}$ but only for the earliest stage; after 10 min of mineralization, only small particles with a diameter of about 10 nm were observed (Fig. 7E), followed by the formation of amorphous globular particles (diameter $\sim 200 \text{ nm}$) after 60 min (Fig. 7F). The rest of the process is different. These amorphous spheroids underwent, indeed, noticeable morphological and structural changes. After 235 min of mineralization, two different morphologies were observed in the same sample (on the same TEM grid). The first morphology (Fig. 7G) consists of poorly crystalline particles with a discernable core-shell structure with an average diameter of 200 nm. Interestingly enough, these globular particles are surrounded by few platelet-shaped structures (see arrow in Fig. 7G) which are most probably made of HAP crystals, as suggested by the SAED pattern (Fig. S5A and B, Supporting information). The second morphology (Fig. 7H) consists of well-defined platelet-shaped structures which clearly exhibited (-141) and (022) diffractions planes of DCPD phase in the SAED pattern (Fig. 7H, inset).

The above findings suggest that, while the very early stages seem to display a similar process involving the formation of amorphous globular particles, the following steps of the crystallization pathway strongly depend on the initial concentration of the substrate. The TEM observations confirm hence the discrepancies unveiled by DLS, even if these observations were limited by multiple scattering.

A particular attention has been dedicated to the core-shell CaP nano-objects. Fig. 8 presents their typical morphology in TEM micrograph and the corresponding elemental maps made with EDX for phosphorus, calcium, oxygen and nitrogen. It is clearly shown that phosphorus, calcium and oxygen are distributed within the particles into a core and a shell phases displaying different electronic densities but both being wholly composed of CaP compounds (Fig. 8A-D). It is noteworthy that the lighter areas (the core of the particles) are unlikely to be composed of an organic phase (e.g. proteins), since no accumulation of nitrogen (Fig. 8E) nor carbon (not shown) were measured in the core: these elements were found to be rather evenly distributed, which can be interpreted as a localization within a layer of adsorbed proteins. XRD diffractogram provides additional information regarding the nature of the CaP compounds present in this sample, and reveals the presence of typical diffraction peaks corresponding to three different crystalline phases: DCPD, Whitlockite (WH) and HAP (Fig. 9). While DCPD and HAP were clearly observed in TEM micrographs (see Fig. 7H, and Fig. 7G (arrow), respectively) and well-identified by SAED, particles of WH were not observed in TEM micrographs nor detected in SAED patterns (WH nano-objects generally exhibit rhombohedral shape [37]) This may be due to their low amount as suggested by the XRD pattern (see intensity ratio of (020) and (214) diffraction planes of DCPD and WH, respectively, Fig. 9).

The globular particles presented in Fig. 7G and 8 are most probably poorly crystalline, even amorphous. This is supported by the fact that no noticeable spots were observed in the SAED pattern when platelets were not clearly visible in the TEM micrograph (Fig. S5C and D, Supporting information). The presence of HAP platelets on the surface of these core-shell nano-objects suggests the growth of crystalline HAP from an amorphous phase. This observation is consistent with previous ones showing the direct transformation of spheroid-

shaped particles of amorphous calcium phosphate to crystalline HAP platelets in aqueous solution [31] or in confined medium. [38]

The previous studies of the mechanism of HAP crystallization at near-physiological conditions have led to a body of knowledge regarding the crystallization pathway from supersaturation solution. Particularly, at early stage, the formation as an intermediate of an amorphous phase, namely ACP, is now well-documented.[4,39] Further characterization regarding the morphology and the composition of this amorphous intermediate has been recently reported by Habraken *et al.* [40]. By using cryogenic TEM experiments, the authors have observed that, during the first minutes, nanometer-sized clusters started to appear and subsequently aggregated to form branched three dimensional polymeric structures which yielded globular particles. The latter turned out to be amorphous calcium phosphate and converted into plate-shaped crystals of HAP after maturation. Similarly, Tang *et al.* have thoroughly investigated the mechanism of nucleation and the kinetics of HAP crystallization from amorphous calcium phosphate phase [31,41–44]. The authors observed amorphous particles aggregated into branched polymeric structures which crystallize progressively into platelet-shaped HAP. In the present study, we also observed the evolution of spheroid-shaped amorphous particles into needle- then platelet-like structures when using the enzyme-induced mineralization at $[S] = 0.7$ mM (Fig. 7A-D). At $[S] = 7.0$ mM ACP particles with similar globular shape were also observed but the following steps of the enzyme-induced mineralization are different: DCPD with WH (Fig. 9) were observed, and the growth of HAP platelets occurred directly on a presumably amorphous phase exhibiting a core-shell structure. As already highlighted in many papers, the initial formation of a DCPD phase can be understood, as its formation is kinetically favored over that of HAP or OCP.[9] This can be explained especially by the low surface tension of DCPD crystals compared to the other CaP structures.[45] Then DCPD progressively dissolves to transform into a thermodynamically

more stable crystalline structure, HAP. It is also well known that, at physiological pH, DCPD is more soluble than HAP.[9]

The presence of Mg^{2+} ions in the medium may influence the crystallization process. Indeed, the kinetics of growth of CaP in the presence of Mg^{2+} ions has been investigated in different conditions, including at constant physiological pH. It has been suggested that Mg^{2+} kinetically delay the growth of HAP, by stabilizing the amorphous precursor (see ref [11] and references therein). However, the precise mechanism by which Mg^{2+} ions act to stabilize the ACP phase is difficult to elucidate, owing to the multiplicity of experimental parameters influencing this process [46–50]. Here, the effect of Mg^{2+} ions was investigated at three concentrations of Mg^{2+} corresponding to those used in the *Ez* procedure, i.e. 0.7, 7.0 and 70 mM. CaP crystallization was initiated by adding Ca^{2+} together with Mg^{2+} and HPO_4^{2-} ions following the procedure described above (*Chem* procedure). After 24 h of mineralization, TEM micrographs did not show noticeable effect on the morphology of the obtained nano-objects for Mg^{2+} concentrations of 0.7 and 7.0 mM (Fig. S6A and B, Supporting information). The latter mostly exhibit flat rod-like structure, as observed without Mg^{2+} ions (see Fig. 1A), but their mean lengths were lower: 44.8 ± 8.9 nm and 37.8 ± 6.6 nm at 0.7 and 7.0 mM, respectively. Besides, the typical diffraction rings observed in the SAED patterns confirm that they are made of crystalline HAP. By contrast, at higher concentration of Mg^{2+} , 70 mM, highly aggregated amorphous particles were observed (Fig. S6C), similarly to those obtained with the *Ez* procedure at $[S] = 70$ mM (Fig. 2H). These findings confirm the role of Mg^{2+} ions to stabilize the amorphous phase in the studied conditions, but only at high concentrations (70 mM). At 0.7 and 7.0 mM, Mg^{2+} ions had only a little impact on the process of HAP crystallization.

The presence of Mg^{2+} ions may also influence the formation of DCPD, detected at $[S] = 7.0$ mM after 235 min of mineralization (Fig. 7H). This strongly depends on the experimental

parameters, particularly pH and ionic strength and the composition of the solution. For instance, it has been reported that, depending on the supersaturation, DCPD may form at a wide range of pH, or dissolve to grow to the more stable WH or HAP phases. [48]. In the present study, as orthophosphate ions are generated *in situ* enzymatically, the supersaturation varies as a function of time, and thus comparisons with previous investigations are difficult to make.

Besides, it appears that enzymes also play a role in the crystallization process. During the first minutes of the process, the DLS size distribution peak of the enzyme dispersed in solution disappeared, suggesting these proteins could have adsorbed onto small particles that just nucleated. Evidence of this adsorption could also be found in the analyses recorded on the final CaP compounds by IR (amide bands, Fig. 4) and XPS (quantitative relationships between data consistent with proteins, Fig. S2, Supporting information). It is worth noting that the presence of proteins in the apatite lattice was not observed. Moreover, as the final CaP compounds were washed three times through centrifugation before drying, this indicates an irreversible adsorption of proteins. The presence of this outer layer of proteins adsorbed at the surface of the CaP particles was also evidenced in an intermediate stage by the elementary analysis (Fig. 8E) and XPS data (Fig. 8F and Fig. S2, Supporting information).

The various availabilities of substrate in solution in the different conditions could be one of the causes of different adsorptions for each of the *Ez* conditions investigated here. The adsorption of the enzymes can be expected to have an important influence on the crystallization process. Indeed, in the manner of polyelectrolytes,[51–54] the adsorption of enzymes is likely to change the surface tension of the crystals, their respective accessibilities to new substrates and their colloidal stability, thus deeply modifying their mechanism and rate of growth.

The results described in the present study raise the question of the role and fate of CaP intermediates which form during the crystallization of HAP, particularly when proteins are present in the media. Moreover, the generation of orthophosphate ions *in situ* is expected to influence the rate of crystallization. This is particularly important because the order of CaP mineralization is governed by both thermodynamic and kinetic considerations.[55] Here, it is shown that the enzyme-induced mineralization follows the Ostwald's rule of stages, as broadly observed for the CaP crystallization from supersaturated solutions in abiotic conditions.[56] In other words, the initial phase that forms is the one with the highest solubility (presumably the amorphous phase here). The pathway to the final crystal phase (HAP in this case) follow, then, a succession of crystalline phase in order of decreasing solubility (DCPD and WH). Interestingly enough, a closer look to the intermediate phases, namely DCPD and WH, opens new prospects for the elucidation of the mechanism of CaP crystallization, as these phases are detected during pathological mineralization.[2,57] At the same time, the growth of HAP platelets was observed to occur directly on globular nano-objects with core-shell structure, presumably amorphous. These findings raise the question of the possible multiplicity of pathways in the process of HAP crystallization, particularly at early stages during *in vivo* mineralization.

4. Conclusion

In this work, the role of an enzyme (ALP) on the crystallization of CaP was investigated to bridge the gap between investigations about *in vivo* biomineralization processes and *in vitro* crystallization in near-physiological conditions. In order to fully characterize the specificities of the enzyme-induced mineralization processes, experiments were performed to study the structure of the final solids obtained through this system. Besides, the *in situ* monitoring of the growth process by DLS allowed to pinpoint characteristic intermediate stages that were

then isolated and characterized to understand better the specificities of the mineralization process due to the use of enzymes.

Indeed, the addition of these proteins turned out to introduce several noticeable alterations in comparison with the chemical process. (i) The dimensions of the final objects obtained through an enzyme-induced process proved to be sensitive to the initial substrate concentration. (ii) These different conditions were showed to lead to different crystallization pathways, where various intermediate phases could be identified. (iii) The role of the enzymes was then established to be probably twofold: on one hand, they allow a fine control of the generation of the CaP precursors and, on the other hand, they fine-tune the growth mechanism of the minerals by adsorbing at their surface, in the manner of polyelectrolytes.

Furthermore, the discovery of DCPD and WH phases intermediately formed during this process paves the way to promising studies. Indeed, these phases were also detected in some pathological mineralization.

Acknowledgments

The authors thank Wiam Belayachi (LRS, Sorbonne University) for her technical assistance for enzyme assay, Caroline Lefebvre (SAPC, UTC) for help in TEM and EDX analyses, Dr. Jean-Marc Kraft for help in DRIFT analyses, and Prof. Claude Jolivald (LRS, Sorbonne University) for the access to UV-Vis spectrophotometer with temperature control and for fruitful discussion.

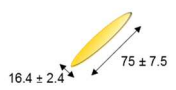
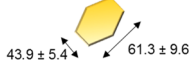
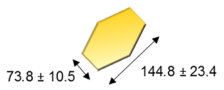
References

- [1] J.S. Al-Sanabani, A.A. Madfa, F.A. Al-Sanabani, Application of Calcium Phosphate Materials in Dentistry, *International Journal of Biomaterials*. 2013 (2013) 12.
- [2] J. Zhang, L. Wang, C.V. Putnis, Underlying Role of Brushite in Pathological Mineralization of Hydroxyapatite, *J. Phys. Chem. B*. 123 (2019) 2874–2881.
- [3] M. Mahjoub, F. Berenbaum, X. Houard, Why subchondral bone in osteoarthritis? The importance of the cartilage bone interface in osteoarthritis, *Osteoporosis International*. 23 (2012) 841–846.
- [4] L. Wang, G.H. Nancollas, Calcium Orthophosphates: Crystallization and Dissolution, *Chem. Rev.* 108 (2008) 4628–4669.
- [5] M. Sadat-Shojai, M.-T. Khorasani, E. Dinpanah-Khoshdargi, A. Jamshidi, Synthesis methods for nanosized hydroxyapatite with diverse structures, *Acta Biomaterialia*. 9 (2013) 7591–7621.
- [6] S.-S. Jee, T.T. Thula, L.B. Gower, Development of bone-like composites via the polymer-induced liquid-precursor (PILP) process. Part 1: Influence of polymer molecular weight, *Acta Biomaterialia*. 6 (2010) 3676–3686.
- [7] M. Maas, P. Guo, M. Keeney, F. Yang, T.M. Hsu, G.G. Fuller, C.R. Martin, R.N. Zare, Preparation of Mineralized Nanofibers: Collagen Fibrils Containing Calcium Phosphate, *Nano Letters*. 11 (2011) 1383–1388.
- [8] H. Zhou, J. Lee, Nanoscale hydroxyapatite particles for bone tissue engineering, *Acta Biomaterialia*. 7 (2011) 2769–2781.
- [9] M.S.-A. Johnsson, G.H. Nancollas, The Role of Brushite and Octacalcium Phosphate in Apatite Formation, *Critical Reviews in Oral Biology & Medicine*. 3 (1992) 61–82.
- [10] A. Lotsari, A.K. Rajasekharan, M. Halvarsson, M. Andersson, Transformation of amorphous calcium phosphate to bone-like apatite, *Nature Communications*. 9 (2018) 4170.
- [11] R. Gelli, F. Ridi, P. Baglioni, The importance of being amorphous: calcium and magnesium phosphates in the human body, *Advances in Colloid and Interface Science*. 269 (2019) 219–235.
- [12] A. Carino, C. Ludwig, A. Cervellino, E. Müller, A. Testino, Formation and transformation of calcium phosphate phases under biologically relevant conditions: Experiments and modelling, *Acta Biomaterialia*. 74 (2018) 478–488.
- [13] J. An, S. Leeuwenburgh, J. Wolke, J. Jansen, 4 - Mineralization processes in hard tissue: Bone, in: C. Aparicio, M.-P. Ginebra (Eds.), *Biom mineralization and Biomaterials*, Woodhead Publishing, Boston, 2016: pp. 129–146.
- [14] E.E. Golub, Role of matrix vesicles in biomineralization, *Biochimica et Biophysica Acta (BBA) - General Subjects*. 1790 (2009) 1592–1598.
- [15] F. Nudelman, K. Pieterse, A. George, P.H.H. Bomans, H. Friedrich, L.J. Brylka, P.A.J. Hilbers, G. de With, N.A.J.M. Sommerdijk, The role of collagen in bone apatite formation in the presence of hydroxyapatite nucleation inhibitors, *Nature Materials*. 9 (2010) 1004–1009.
- [16] E.E. Golub, K. Boesze-Battaglia, The role of alkaline phosphatase in mineralization, *Current Opinion in Orthopaedics*. 18 (2007). https://journals.lww.com/co-ortho/Fulltext/2007/09000/The_role_of_alkaline_phosphatase_in_mineralization.5.aspx.
- [17] A. Sabokbar, P.J. Millett, B. Myer, N. Rushton, A rapid, quantitative assay for measuring alkaline phosphatase activity in osteoblastic cells in vitro, *Bone and Mineral*. 27 (1994) 57–67.
- [18] E.E. Golub, Role of matrix vesicles in biomineralization, *Biochimica et Biophysica Acta (BBA) - General Subjects*. 1790 (2009) 1592–1598.
- [19] H. Anderson, R. Garimella, S. Tague, The role of matrix vesicles in growth plate development and biomineralization, *Frontiers in Bioscience : A Journal and Virtual Library*. 10 (2005) 822–37.
- [20] N. Rauner, M. Meuris, M. Zoric, J.C. Tiller, Enzymatic mineralization generates ultrastiff and tough hydrogels with tunable mechanics, *Nature*. 543 (2017) 407.

- [21] S.K. Samal, M. Dash, H.A. Declercq, T. Gheysens, J. Dendooven, P.V.D. Voort, R. Cornelissen, P. Dubruel, D.L. Kaplan, Enzymatic Mineralization of Silk Scaffolds, *Macromolecular Bioscience*. 14 (2014) 991–1003.
- [22] T.E.L. Douglas, P.B. Messersmith, S. Chasan, A.G. Mikos, E.L.W. de Mulder, G. Dickson, D. Schaubroeck, L. Balcaen, F. Vanhaecke, P. Dubruel, J.A. Jansen, S.C.G. Leeuwenburgh, Enzymatic Mineralization of Hydrogels for Bone Tissue Engineering by Incorporation of Alkaline Phosphatase, *Macromolecular Bioscience*. 12 (2012) 1077–1089.
- [23] A. Aminian, K. Pardun, E. Volkmann, G. Li Destri, G. Marletta, L. Treccani, K. Rezwani, Enzyme-assisted calcium phosphate biomineralization on an inert alumina surface, *Acta Biomaterialia*. 13 (2015) 335–343.
- [24] M. Michel, Y. Arntz, G. Fleith, J. Toquant, Y. Haikel, J.-C. Voegel, P. Schaaf, V. Ball, Layer-by-Layer Self-Assembled Polyelectrolyte Multilayers with Embedded Liposomes: Immobilized Submicronic Reactors for Mineralization, *Langmuir*. 22 (2006) 2358–2364.
- [25] H.H. Hsu, P.A. Munoz, J. Barr, I. Oppliger, D.C. Morris, H.K. Vaananen, N. Tarkenton, H.C. Anderson, Purification and partial characterization of alkaline phosphatase of matrix vesicles from fetal bovine epiphyseal cartilage. Purification by monoclonal antibody affinity chromatography., *Journal of Biological Chemistry*. 260 (1985) 1826–1831.
- [26] H.N. Fernley, P.G. Walker, Studies on alkaline phosphatase. Inhibition by phosphate derivatives and the substrate specificity, *Biochem J*. 104 (1967) 1011–1018.
- [27] D. Chappellet-Tordo, M. Fosset, M. Iwatsubo, C. Gache, M. Lazdunski, Intestinal alkaline phosphatase. Catalytic properties and half of the sites reactivity, *Biochemistry*. 13 (1974) 1788–1795.
- [28] M.F. Hoylaerts, T. Manes, J.L. Millán, Mammalian Alkaline Phosphatases Are Allosteric Enzymes, *Journal of Biological Chemistry*. 272 (1997) 22781–22787.
- [29] Liga Berzina-Cimdina, Research of Calcium Phosphates Using Fourier Transform Infrared Spectroscopy, in: Natalija Borodajenko ED1 - Theophile Theophanides (Ed.), *Infrared Spectroscopy*, IntechOpen, Rijeka, 2012: p. Ch. 6.
- [30] S. Koutsopoulos, Synthesis and characterization of hydroxyapatite crystals: A review study on the analytical methods, *Journal of Biomedical Materials Research*. 62 (2002) 600–612.
- [31] S. Jiang, H. Pan, Y. Chen, X. Xu, R. Tang, Amorphous calcium phosphate phase-mediated crystal nucleation kinetics and pathway, *Faraday Discuss*. 179 (2015) 451–461.
- [32] H. Maachou, M.J. Genet, D. Aliouche, C.C. Dupont-Gillain, P.G. Rouxhet, XPS analysis of chitosan–hydroxyapatite biomaterials: from elements to compounds, *Surface and Interface Analysis*. 45 (2013) 1088–1097.
- [33] J. Landoulsi, M.J. Genet, C. Richard, K. El Kirat, S. Pulvin, P.G. Rouxhet, Evolution of the passive film and organic constituents at the surface of stainless steel immersed in fresh water, *Journal of Colloid and Interface Science*. 318 (2008) 278–289.
- [34] M.J. Genet, C.C. Dupont-Gillain, P.G. Rouxhet, XPS Analysis of Biosystems and Biomaterials, in: *Medical Applications of Colloids*, Egon Matijević, USA, 2008.
- [35] J. Landoulsi, M.J. Genet, S. Fleith, Y. Touré, I. Liascukiene, C. Méthivier, P.G. Rouxhet, Organic adlayer on inorganic materials: XPS analysis selectivity to cope with adventitious contamination, *Applied Surface Science*. 383 (2016) 71–83.
- [36] I.S. Harding, N. Rashid, K.A. Hing, Surface charge and the effect of excess calcium ions on the hydroxyapatite surface, *Biomaterials*. 26 (2005) 6818–6826.
- [37] H.L. Jang, K. Jin, J. Lee, Y. Kim, S.H. Nahm, K.S. Hong, K.T. Nam, Revisiting Whitlockite, the Second Most Abundant Biomineral in Bone: Nanocrystal Synthesis in Physiologically Relevant Conditions and Biocompatibility Evaluation, *ACS Nano*. 8 (2014) 634–641.
- [38] A. Lotsari, A.K. Rajasekharan, M. Halvarsson, M. Andersson, Transformation of amorphous calcium phosphate to bone-like apatite, *Nature Communications*. 9 (2018) 4170.
- [39] R. Gelli, F. Ridi, P. Baglioni, The importance of being amorphous: calcium and magnesium phosphates in the human body, *Advances in Colloid and Interface Science*. 269 (2019) 219–235.

- [40] W.J.E.M. Habraken, J. Tao, L.J. Brylka, H. Friedrich, L. Bertinetti, A.S. Schenk, A. Verch, V. Dmitrovic, P.H.H. Bomans, P.M. Frederik, J. Laven, P. van der Schoot, B. Aichmayer, G. de With, J.J. DeYoreo, N.A.J.M. Sommerdijk, Ion-association complexes unite classical and non-classical theories for the biomimetic nucleation of calcium phosphate, *Nature Communications*. 4 (2013) 1507.
- [41] S. Jiang, W. Jin, Y.-N. Wang, H. Pan, Z. Sun, R. Tang, Effect of the aggregation state of amorphous calcium phosphate on hydroxyapatite nucleation kinetics, *RSC Adv*. 7 (2017) 25497–25503.
- [42] J. Tao, H. Pan, Y. Zeng, X. Xu, R. Tang, Roles of Amorphous Calcium Phosphate and Biological Additives in the Assembly of Hydroxyapatite Nanoparticles, *J. Phys. Chem. B*. 111 (2007) 13410–13418.
- [43] H. Pan, X.Y. Liu, R. Tang, H.Y. Xu, Mystery of the transformation from amorphous calcium phosphate to hydroxyapatite, *Chem. Commun*. 46 (2010) 7415–7417.
- [44] S. Jiang, Y. Chen, H. Pan, Y.-J. Zhang, R. Tang, Faster nucleation at lower pH: amorphous phase mediated nucleation kinetics, *Phys. Chem. Chem. Phys*. 15 (2013) 12530–12533.
- [45] G.H. Nancollas, W. Wu, Biomineralization mechanisms: a kinetics and interfacial energy approach, *Journal of Crystal Growth*. 211 (2000) 137–142.
- [46] A.L. Boskey, A.S. Posner, Magnesium stabilization of amorphous calcium phosphate: A kinetic study, *Materials Research Bulletin*. 9 (1974) 907–916.
- [47] F. Abbona, A. Baronnet, A XRD and TEM study on the transformation of amorphous calcium phosphate in the presence of magnesium, *Journal of Crystal Growth*. 165 (1996) 98–105.
- [48] F. Abbona, M. Franchini-Angela, Crystallization of calcium and magnesium phosphates from solutions of low concentration, *Journal of Crystal Growth*. 104 (1990) 661–671.
- [49] W. Kibalczyk, J. Christoffersen, M.R. Christoffersen, A. Zielenkiewicz, W. Zielenkiewicz, The effect of magnesium ions on the precipitation of calcium phosphates, *Journal of Crystal Growth*. 106 (1990) 355–366.
- [50] M.H. Salimi, J.C. Heughebaert, G.H. Nancollas, Crystal growth of calcium phosphates in the presence of magnesium ions, *Langmuir*. 1 (1985) 119–122.
- [51] B. Cantaert, E. Beniash, F.C. Meldrum, The role of poly(aspartic acid) in the precipitation of calcium phosphate in confinement, *Journal of Materials Chemistry B*. 1 (2013) 6586.
- [52] A. Shkilnyy, A. Friedrich, B. Tiersch, S. Schöne, M. Fechner, J. Koetz, C.-W. Schläpfer, A. Taubert, Poly(ethylene imine)-Controlled Calcium Phosphate Mineralization, *Langmuir*. 24 (2008) 2102–2109.
- [53] R.J. Coleman, K.S. Jack, S. Perrier, L. Grøndahl, Hydroxyapatite Mineralization in the Presence of Anionic Polymers, *Crystal Growth & Design*. 13 (2013) 4252–4259.
- [54] P.B.-Y. Ofir, R. Govrin-Lippman, N. Garti, H. Füredi-Milhofer, The Influence of Polyelectrolytes on the Formation and Phase Transformation of Amorphous Calcium Phosphate, *Crystal Growth & Design*. 4 (2004) 177–183.
- [55] L. Wang, G.H. Nancollas, Pathways to biomineralization and biomineralization of calcium phosphates: the thermodynamic and kinetic controls, *Dalton Trans*. (2009) 2665–2672.
- [56] G.H. Nancollas, *Biological Mineralization and Demineralization*, Springer, G.H. Nancollas, New York, 1981.
- [57] C.A. Scotchford, S.Y. Ali, Magnesium whitlockite deposition in articular cartilage: a study of 80 specimens from 70 patients., *Ann Rheum Dis*. 54 (1995) 339.

Table 1. Characteristics of calcium phosphate compounds formed after 24 h via *Chem* and *Ez* procedures (pH 7.4; 37 °C).

	<i>Chem</i>	<i>Ez</i> [S] = 0.7 mM	<i>Ez</i> [S] = 7.0 mM	<i>Ez</i> [S] = 70 mM
Shape	Flat rod	Platelet	Platelet	
Dimensions (nm) *				Not defined
AR †	4.6	1.4	1.9	
Crystal phase ‡	HAP	HAP	HAP	
% crystallinity §	0.62	0.41	0.53	Amorphous

* Determined from TEM micrographs (size distribution of 100 nano-objects for each system)

† AR = aspect ratio

‡ Determined from XRD data

§ Index of crystallinity = $(I_{002} - I_{bgr})/I_{002}$

Table 2. XPS analysis of CaP compounds obtained via the *Chem* or *Ez* procedure: surface concentration (mole fraction with respect to all elements except hydrogen, %) of elements and of groups defined by the binding energy of peak components

	C 1s					N 1s	O 1s			Ca 2p	P 2p	Mg 2s
	C-(C,H)	C-(O, N)	C=O, O-C-O	C-(C=O)-O, O-(C=O)-O	C _{tot}	C-N	C=O P=O P-O	C-OH P-OH	O _{tot}			
	BE (eV)	284.8	286.3	288.0	289.0	400.0	531.0	532.5		347.2*	133.0*	88.8
<i>Chem</i>	7.32	2.88	1.10	1.25	12.55	0.40	42.93	5.02	47.94	20.72	18.39	bdl
<i>Ez</i> -0.7 mM	21.92	13.28	7.59	1.47	44.26	6.68	23.34	7.02	30.36	9.97	8.73	bdl
<i>Ez</i> -7.0 mM	9.33	7.26	3.70	0.87	21.14	2.88	35.63	6.64	42.26	16.77	16.09	0.85
<i>Ez</i> -70 mM	8.51	8.05	2.63	1.26	20.44	1.04	34.54	10.26	44.81	7.97	16.13	9.62

* binding energy given for the 2p_{3/2} component; bdl=below the detection limit

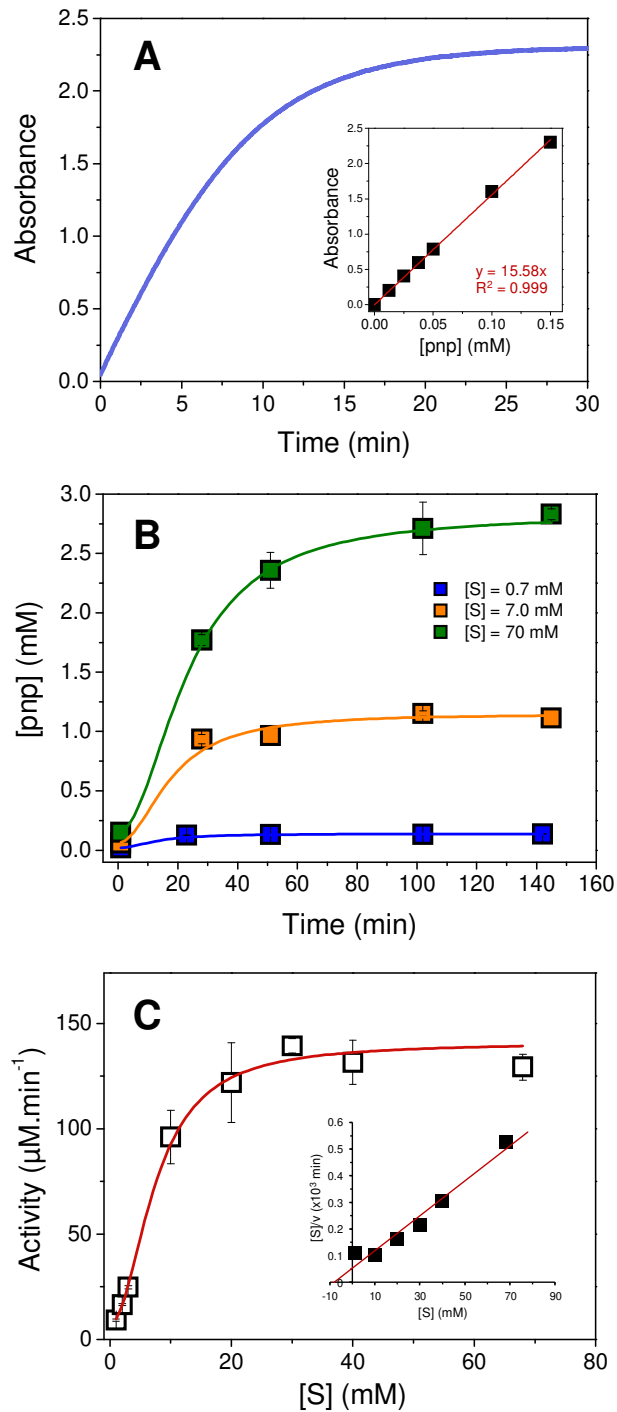


Fig. 1. Measurements of ALP catalytic activity in aqueous solution ($\text{CaCl}_2 = 11.6 \text{ mM}$; $\text{pH} = 7.4$; $37 \text{ }^\circ\text{C}$). (A) Evolution of the absorbance ($\lambda = 410 \text{ nm}$) vs time due to the enzymatic production of pnp (inset: calibration curve relating absorbance to pnp concentration). (B) Kinetics of pnp production over time at different substrate S concentrations: $[S] = 0.7$; 7.0 and 70 mM . (C) Evolution of the catalytic activity (initial velocity, v) as a function of the substrate

S concentration. Straight line is the Hill function, yielding fitting parameters of $K_m = 7.5$ mM and $n = 2$ (inset: $v/[S]$ vs $[S]$ plot showing a linear relationship and yielding a K_m value equal to 8.1 mM).

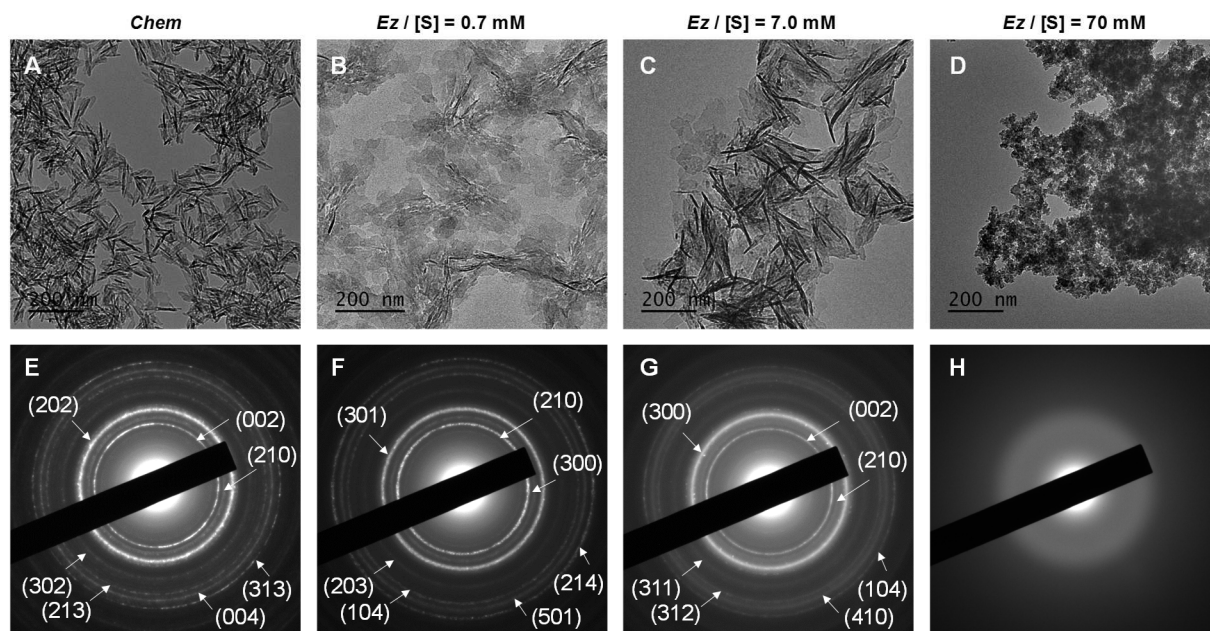


Fig. 2. (A-D) TEM micrographs and (E-H) SAED patterns of calcium phosphate obtained after 24 h at pH 7.4 and 37 °C using (A, E) the chemical (*Chem*) or the enzymatic (*Ez*) procedure at substrate concentration equal to (B, F) 0.7, (C, G) 7.0 or (D, H) 70 mM.

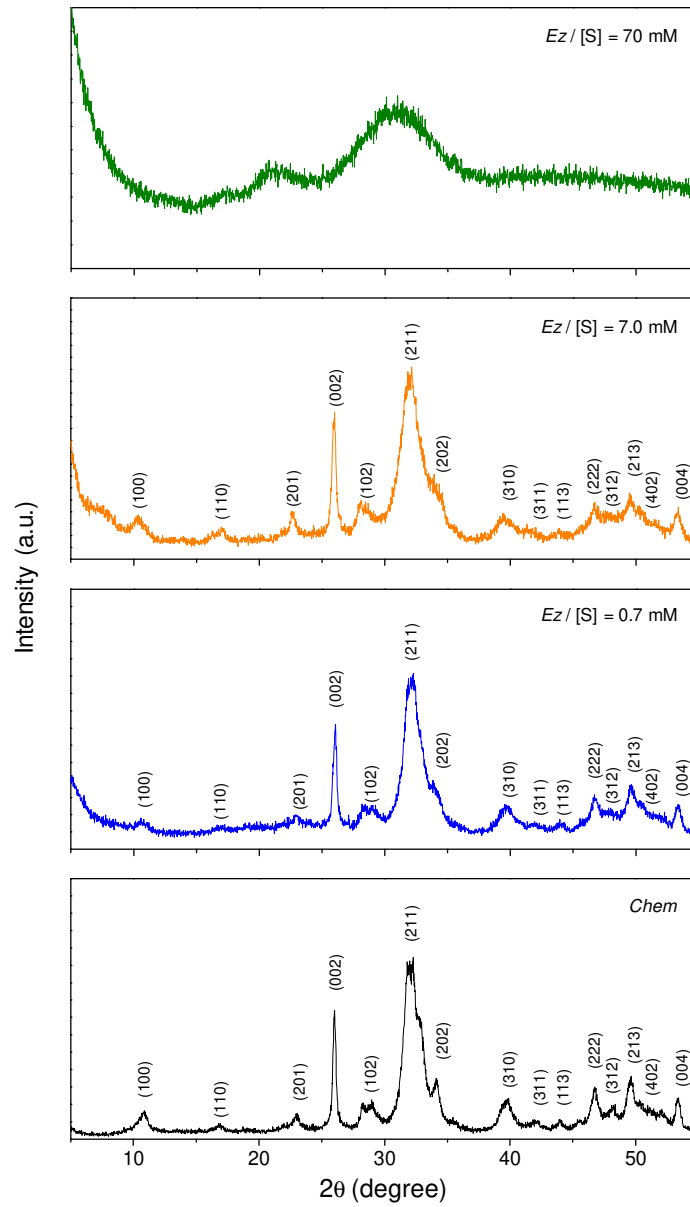


Fig. 3. XRD patterns of calcium phosphate obtained after 24 h at pH 7.4 and 37 °C using the chemical (*Chem*) or the enzymatic (*Ez*) procedure at a substrate concentration $[S] = 0.7; 7.0$ or 70 mM, as indicated.

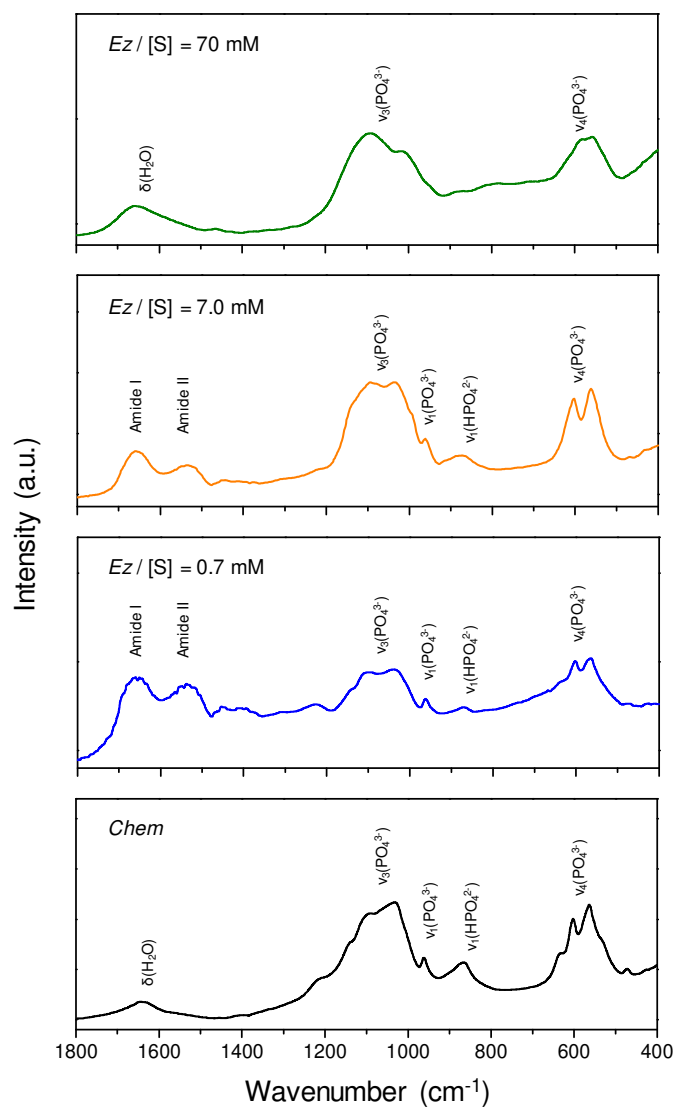


Fig. 4. DRIFT spectra of the calcium phosphate compounds obtained after 24 h at pH 7.4 and 37 °C using *Chem* or *Ez* procedures at different substrate concentrations, as indicated.

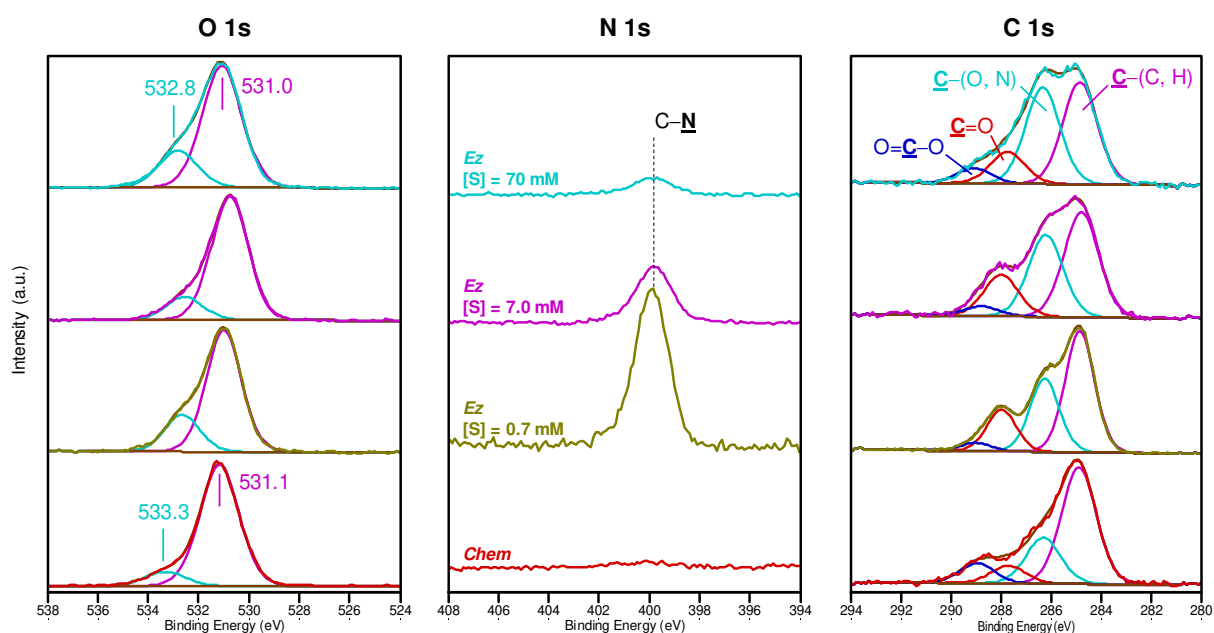


Fig. 5. Decomposition of O 1s, N 1s and C 1s peaks recorded on calcium phosphate obtained after 24 h at pH 7.4 and 37 °C using the chemical (*Chem*) or the enzymatic (*Ez*) procedure at a substrate concentration [S] = 0.7; 7.0 or 70 mM, as indicated.

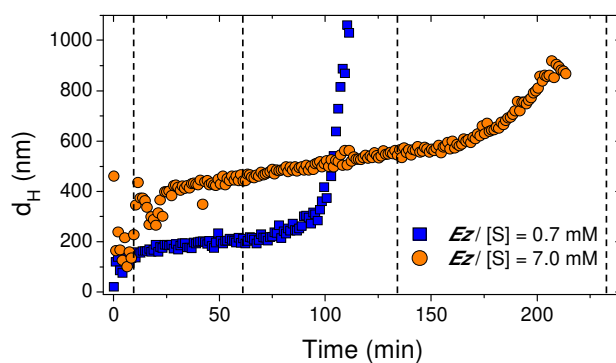


Fig. 6. Hydrodynamic diameter (d_H) measured as a function of time during the enzyme-induced mineralization (pH 7.4, 37 °C) at (blue squares) [S] = 0.7 mM and (orange disks) [S] = 7.0 mM. Dashed lines indicate the characteristic times at which aliquots were withdrawn to get a better insight on the intermediate states and structure.

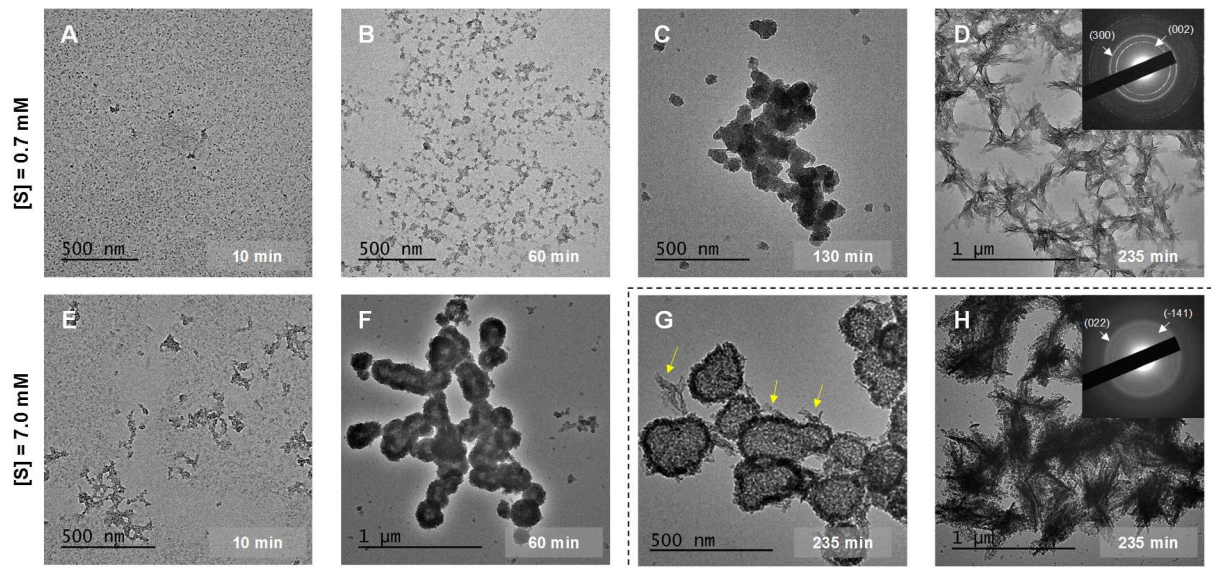


Fig. 7. (A-H) TEM micrographs of calcium phosphate obtained at pH 7.4 and 37 °C using 0.7 mM of substrate in the *Ez* procedure after (A) 10 min, (B) 60 min, (C) 130 min, (D) 235 min and using 7.0 mM of substrate in the *Ez* procedure after (E) 10 min, (F) 60 min, (G-H) 235 min. SAED patterns are shown in inset in (D) and (H).

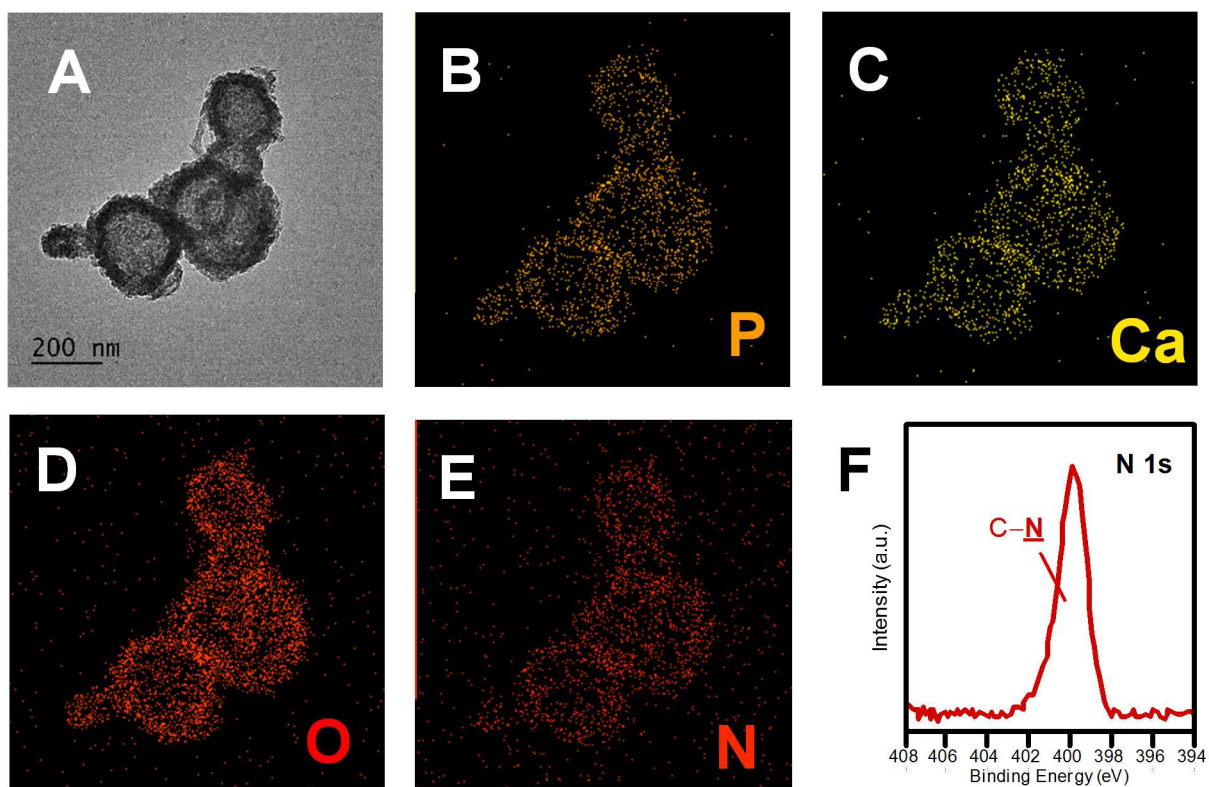


Fig. 8. (A) TEM micrograph of calcium phosphate obtained after 235 min at pH 7.4 and 37 °C using the *Ez* procedure at [S] = 7.0 mM with the corresponding elemental maps of (B) phosphorus, (C) calcium, (D) oxygen and (E) nitrogen. (F) Typical N 1s XPS peak recorded on the same sample.

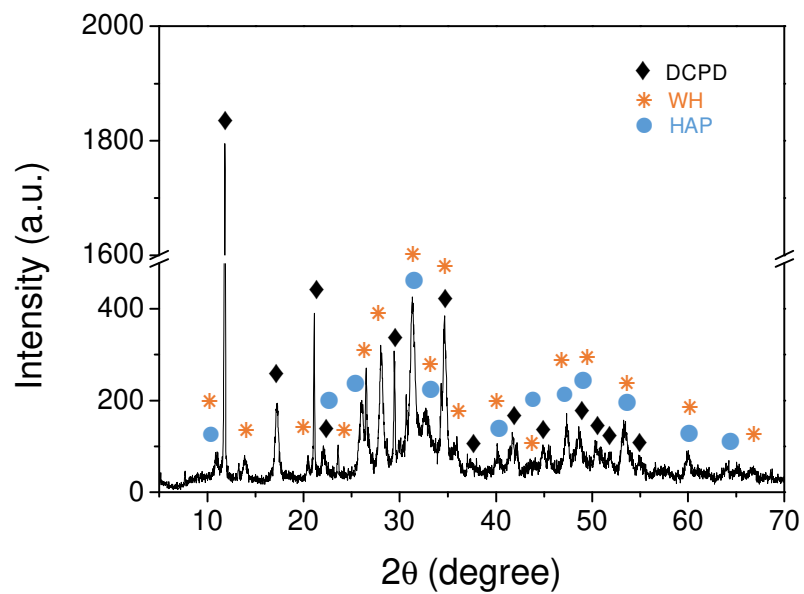


Fig. 9. XRD pattern of calcium phosphate obtained after 235 min at pH 7.4 and 37 °C using the E_z procedure at $[S] = 7.0$ mM.

